+ MODEL

Genes & Diseases (2024) 11, 101009

Available online at www.sciencedirect.com

ScienceDirect

journal homepage: www.keaipublishing.com/en/journals/genes-diseases

FULL LENGTH ARTICLE

Cerebral furin deficiency causes hydrocephalus in mice

Shiqi Xie [a,1], Xiaoyong Xie [b,1], Jing Tang [b], Biao Luo [b], Jian Chen [b], Qixin Wen [b], Jianrong Zhou [a,*], Guojun Chen [b,**]

[a] *Nursing College, Chongqing Medical University, Chongqing 400016, China*
[b] *Department of Neurology, The First Affiliated Hospital of Chongqing Medical University, Chongqing Key Laboratory of Major Neurological and Mental Disorders, Chongqing Key Laboratory of Neurology, Chongqing 400016, China*

Received 13 December 2022; received in revised form 20 April 2023; accepted 29 April 2023
Available online 8 July 2023

KEYWORDS
Astrocyte;
Ciliogenesis;
Conditional knockout;
Ependymal;
Furin;
Hydrocephalus;
Proteomics

Abstract Furin is a pro-protein convertase that moves between the trans-Golgi network and cell surface in the secretory pathway. We have previously reported that cerebral overexpression of furin promotes cognitive functions in mice. Here, by generating the brain-specific furin conditional knockout (cKO) mice, we investigated the role of furin in brain development. We found that furin deficiency caused early death and growth retardation. Magnetic resonance imaging showed severe hydrocephalus. In the brain of furin cKO mice, impaired ciliogenesis and the derangement of microtubule structures appeared along with the down-regulated expression of RAB28, a ciliary vesicle protein. In line with the widespread neuronal loss, ependymal cell layers were damaged. Further proteomics analysis revealed that cell adhesion molecules including astrocyte-enriched ITGB8 and BCAR1 were altered in furin cKO mice; and astrocyte overgrowth was accompanied by the reduced expression of SOX9, indicating a disrupted differentiation into ependymal cells. Together, whereas alteration of RAB28 expression correlated with the role of vesicle trafficking in ciliogenesis, dysfunctional astrocytes might be involved in ependymal damage contributing to hydrocephalus in furin cKO mice. The structural and molecular alterations provided a clue for further studying the potential mechanisms of furin.

* Corresponding author.
** Corresponding author.
E-mail addresses: 236809246@qq.com (J. Zhou), woodchen2015@163.com (G. Chen).
Peer review under responsibility of Chongqing Medical University.
[1] These authors contributed equally to this work.

https://doi.org/10.1016/j.gendis.2023.04.037

Introduction

Hydrocephalus is a common birth disorder with an estimated incidence of 1 in 1000 newborns.[1] Structural and genetic factors cause abnormalities in the flow of cerebrospinal fluid (CSF), leading to an enlargement of the cerebral ventricles.[2,3] Many of the gene mutations are associated with growth factors, cell surface molecules, and intracellular signaling.[2] These molecular alterations correlate with ependymal denudation, cilia disruption, gliosis, and inflammation.[4,5]

Furin is a precursor protein convertase.[6] In the secretory pathway, furin is trafficked from the trans-Golgi network to the cell surface and processes a variety of substrates ranging from growth factors, matrix metalloproteinases, and receptors to viral-envelope glycoproteins and bacterial exotoxins.[7] A large body of evidence indicates that furin is involved in viral infection,[8,9] tumor metastasis,[10] cardiovascular,[11] and neurological diseases.[12,13] In the brain of mice, overexpression of furin promotes dendritic morphogenesis and cognitive function[14] but also contributes to epileptic susceptibility.[15] Given that furin knockout mice are embryonic lethal,[16] how furin regulates the development of the brain is not completely understood.

In this study, we generated a conditional knockout (cKO) mouse model by targeting the brain-specific furin. We defined that furin deficiency causes early death and growth retardation. The development of hydrocephalus was paralleled with the impaired ciliogenesis and ependymal cells that form the lining of the lateral ventricles. We further found that the vesicle protein RAB28 was associated with impaired ciliogenesis, and the astrocyte-enriched cell adhesion molecules could be involved in the abnormal differentiation of astrocytes into ependymal cells.

Materials and methods

Generation of furin cKO mice and tissue preparation

All animal protocols were approved by the Institutional Animal Ethics Committee of the First Affiliated Hospital of Chongqing Medical University, China, in accordance with the NIH Guidelines for the Care and Use of Laboratory Animals.

Furin cKO mice were generated by crossing the floxed furin ($Furin^{f/f}$) mice with Nestin-Cre transgenic mice (The Jackson Laboratory), which expresses Cre recombinase in the nervous system.[17] $Furin^{f/f}$ mice were created on a C57BL/6J background (CasGene Biotech Co., Ltd, Beijing, China). Mouse zygotes obtained by mating males with superovulated females were micro-injected with a mixture of Cas9 mRNA (80 ng/μL), sgRNA (40 ng/μL), and donor vector (8 ng/μL). The injected zygotes were transferred into pseudopregnant CD1 female mice, and viable adult $Furin^{f/f}$ mice were obtained. The correctly targeted mice were genotyped by PCR and sequencing.[18]

Mice were anesthetized by intraperitoneal injection of 2% sodium pentobarbital (50 mg/kg) and intracardially perfused with 20 mL of 0.01 M PBS (pH = 7.4), followed by 150 mL of 4% paraformaldehyde. Then, brain samples were isolated immediately and stored in 4% paraformaldehyde for 24 h at 4 °C before use. For Western blotting, brain tissues without intracardial perfusion were collected and immediately stored in liquid nitrogen.

Quantitative reverse transcription PCR

Total RNA was extracted using the Trizol kit (Takara, Dalian, China), and cDNA was synthesized using the cDNA Synthesis Kit (Vazyme, Nanjing, China). Quantitative reverse transcription PCR and cDNA sequencing were performed following standard methods.[14] Primer sequences were: Furin-seq-F1 TGAGAACCACTGCTCTAGCCTTCC, Furin-seq-R1 AGAGACAACCAGCCCATTACCAGA; Nes-F GCCTTATTGTGGAAGGACTG, Nes-R CCTTCCTGAAGCAGTAGAGCA, respectively.

Western blotting

A RIPA protein extraction kit (Beyotime Biotechnology China) containing phenylmethylsulfonyl fluoride (PMSF; Beyotime Biotechnology China) was used to extract total protein. An enhanced bicinchoninic acid (BCA) protein assay kit (Beyotime Institute of Biotechnology) was used to determine protein concentrations. Western blotting analysis was performed according to published protocols.[19] The following antibodies were used: furin (1:1000, Abcam, ab183495), S100 calcium-binding protein B (S100β) (1:1000, Abcam, ab52642), SRY-Box transcription factor 9 (SOX9) (1:5000, Abcam, ab185966), polypyrimidine tract binding protein 1 (PTBP1) (1:2000, Proteintech, 12582-1-AP), glial fibrillary acidic protein (GFAP) (1:2000, Proteintech, 16825-1-AP), adenylate cyclase 3 (ADCY3) (1:1000, Proteintech, 19492-1-AP), Rab28 (1:1000, Thermo, PA5-68303), NeuN (1:1500, Abcam, ab177487), GAPDH (1:5000, Proteintech, 10494-1-AP), and horseradish peroxidase-conjugated anti-rabbit or anti-mouse secondary antibodies (1:3000, Proteintech). The bands were visualized using Western Bright ECL (Advansta, US) and a Fusion FX5 image analysis system (Vilber Lourmat, France).

Immunofluorescent labeling and immunohistochemistry

For immunofluorescent labeling,[20,21] brain tissues were dehydrated in gradient sucrose solutions. After antigen recovery, tissues were cryo-sectioned (10-μm thickness) by a freezing microtome (Thermo, USA) and permeabilized for 10 min using 0.4% Triton X-100 and blocked using 10% donkey serum (Solarbio, SL050) at 37 °C for 30 min to eliminate nonspecific staining. Then, slices were incubated with the primary antibody mixture at 4 °C overnight, and secondary antibodies in the dark at 37 °C for 2 h. The following primary antibodies were used: furin (1:100, Abcam, ab183495), S100β (1:100, Abcam, ab52642), SOX9 (1:200, Abcam, ab185966), GFAP (1:500, Proteintech, 16825-1-AP), RAB28 (1:100, Thermo, PA5-68303). Images were captured using a laser scanning confocal microscope (Leica TCS SP8 X, Germany). Immunofluorescence intensity and colocalization were quantified using Image-Pro Plus 6.0 software (Media Cybernetics, USA).

For immunocytochemistry, paraffin-embedded tissue sections (10-μm thickness) were dewaxed with xylene and rehydrated in a series of gradient ethanol solutions. After antigen retrieval, a peroxidase inhibitor (PV-9002, ZSGB-BIO) was used to block endogenous peroxidase activity.[22] Tissue sections were then incubated with NeuN antibody (1:100, Abcam, ab177487) at 4 °C overnight, followed by incubation with a biotinylated secondary goat anti-rabbit antibody (1:500, Zhongshan Golden Bridge, Inc.) at 37 °C for 30 min and then an avidin-biotin-peroxidase complex (Zhongshan Golden Bridge) at 37 °C for 30 min. The sections were incubated with 3,3′-diaminobenzidine (Zhongshan Golden Bridge) and hematoxylin. Finally, slices were dehydrated in a series of ethanol solutions and cleared in xylene before being mounted with neutral resin. Images were captured using a LEICA DM6000B automated microscope (Leica, Germany). The Motic Med 6.0 CMIAS pathology image analysis system (Beijing Motic, Beijing, China) was used to perform automatic semi-quantitative analysis on 10 randomly selected images from each section.

Magnetic resonance imaging

Mice at 3 months were anesthetized by 2% isoflurane, and imaged with a 7 T, 20-cm horizontal bore instrument by T1- and T2-weighted modalities at the Small Animal Imaging Facility (Bruker, Germany). Body core temperature was kept at 37 °C by a rectal probe. After completion, the mice were immediately rewarmed under a heat lamp. Ventricle and total brain volumes were quantified by the ITK-SNAP (V3.2) software.[19,23]

Transmission electron microscopy (TEM) and scan electron microscopy (SEM)

Brain tissues were dissected and fixed by a mixture of 2.5% glutaraldehyde and 1% osmium tetroxide at 4 °C overnight before sampling. For TEM, ultra-thin sections (50-nm thickness) were obtained using a Leica EMUC7 ultramicrotome. After being stained with uranyl acetate and lead citrate, sections were imaged using a Hitachi-7500 transmission electron microscope.[24] For SEM, dehydrated sections were coated with gold particles and scanned with a Hitachi SU8O10 scanning electron microscope.[25,26]

Proteomics

Brain tissues from mice at 3 months were lysed in SDT buffer (4% SDS, 100 mM Tris/HCl pH 7.6, 0.1 M DTT) for protein extraction and then quantified by the BCA method. Samples were desalted by C18 Cartridge and then lyophilized and solubilized by adding 40 μL of 0.1% formic acid solution for peptide quantification (OD_{280}). Peptides were labeled according to the instructions of Thermo's TMT labeling kit, and then mixed in equal amounts and graded using the High pH Reversed-Phase Peptide Fractionation Kit. The column was first equilibrated with acetonitrile and 0.1% trifluoroacetic acid, and then the labeled peptides were sampled, desalted by adding pure water, and centrifuged at a low speed. The column-bound peptides were eluted with increasing concentrations of acetonitrile solutions. Each peptide sample was vacuum-dried and then lyophilized with 12 μL of 0.1% formic acid. Each sample was separated using an HPLC liquid phase system with a nanoliter flow rate. Samples were separated by chromatography and then analyzed using a mass spectrometer. Protein identification and quantitative analysis were performed by Database.

Statistical analysis

All statistical analyses were conducted using the statistical software GraphPad Prism 8.0, and data results were biologically repeated at least three times. To determine whether the samples exhibited normal distributions and equal variances (determined by the one-sample Kolmogorov—Smirnov test and Levene's test), the experimental results were statistically assessed using parametric or nonparametric tests. All data were expressed as mean ± standard error of the mean and were analyzed using Student's *t*-test or repeated measures ANOVA. Differences were considered significant when *P*-values <0.05.

Results

Furin deficiency caused growth retardation and early perinatal lethality

Furin protein is highly expressed in the brain, particularly in the cortex and hippocampus.[13] To determine the primary roles of furin in nervous system development, we generated furin conditional knockout mice ($FURIN^{-/-}$), by crossing the floxed furin allele ($FURIN^{f/f}$) with Nestin-Cre (Fig. 1A). In Nestin-Cre mice, Cre recombinase is controlled by a nestin promoter that is expressed in neuronal and glial cell precursors.[27] These $FURIN^{-/-}$ mice were featured by enlarged dome-shaped skulls, but the brain showed no overt gross abnormalities (Fig. 1B). In addition, the postnatal growth of $FURIN^{-/-}$ was retarded as demonstrated by body size that was significantly smaller in $FURIN^{-/-}$ than in $FURIN^{+/-}$ and $FURIN^{+/+}$ mice of the same age (Fig. 1C). As shown in Figure 1D and E, the protein level of furin was significantly decreased in the brain of $FURIN^{-/-}$ mice relative to $FURIN^{+/+}$ mice. Genotyping analysis revealed that the LOXP site was successfully inserted flanking exons 5—6, with the correct expression of Cre in the three different mice (Fig. 1F). Accordingly, furin mRNA levels were dramatically decreased in $FURIN^{-/-}$ mice compared with $FURIN^{+/+}$ mice (Fig. 1G). Most of the $FURIN^{-/-}$ mice were viable at birth. However, $FURIN^{-/-}$ mice failed to thrive with lethargy and muscle weakness, and died early at different times within the first 3 weeks (Fig. 1H). As shown in Figure 1I, $FURIN^{+/-}$ mice behaved similarly to $FURIN^{+/+}$ mice and lived up to 24 months, but exhibited lower body weight, especially at 180 days; whereas only half of $FURIN^{-/-}$ mice survived at 180 days, with a loss of body weight at all stages. These results indicated that furin was essential for postnatal development, growth, and survival.

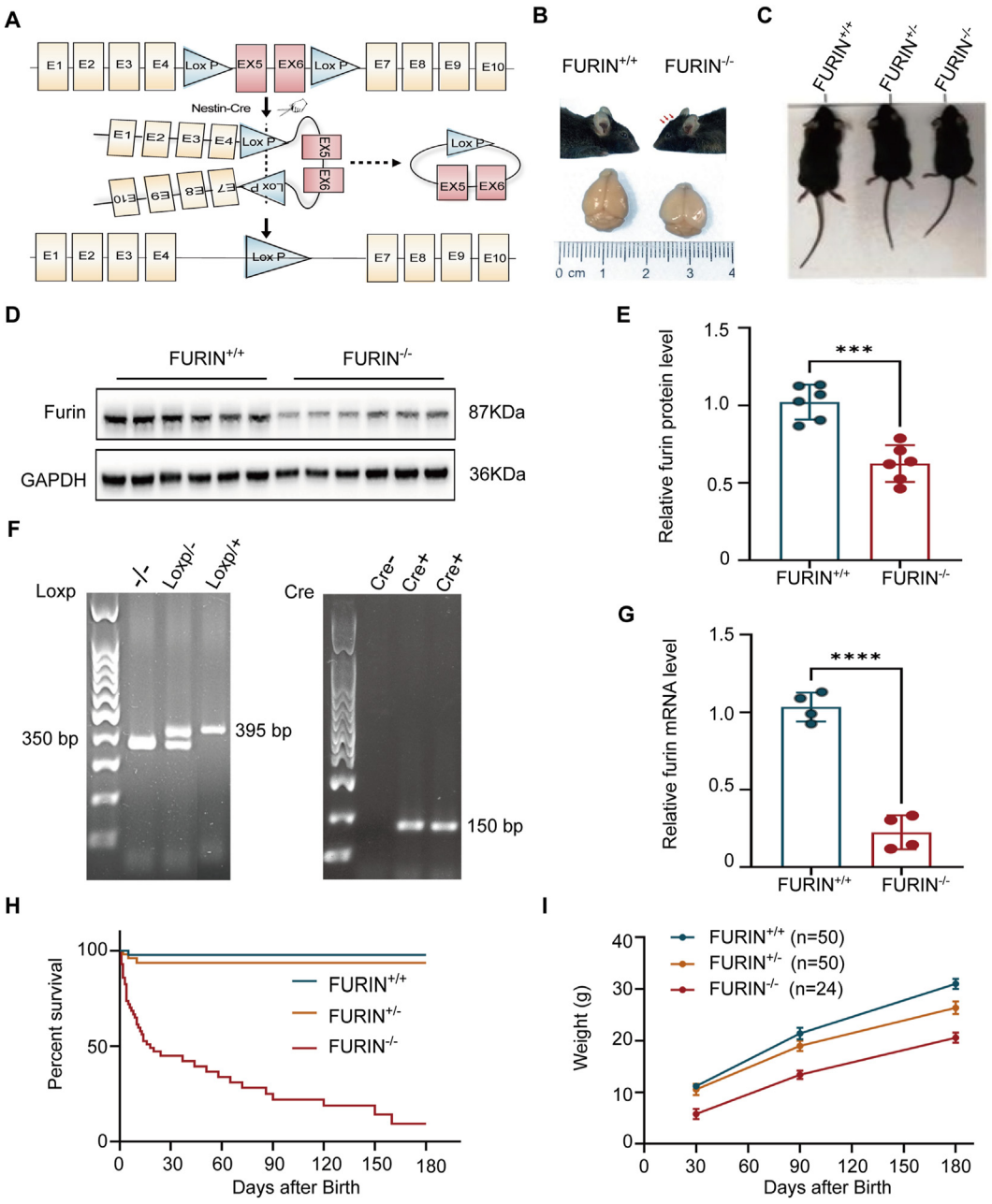

Figure 1 Generation of furin conditional knockout mice. **(A)** Schematic representation of the FURIN gene targeting strategy. The blue triangles of Loxp sites are responsible for eliminating exons 5—6 by Cre recombinase in neurons. **(B)** Representative images of FURIN$^{+/+}$ and FURIN$^{-/-}$ mice at 5 months. Arrows indicate the enlarged and dome-shaped skull. **(C)** Gross appearance of FURIN$^{-/-}$, FURIN$^{+/-}$, and FURIN$^{+/+}$ mice. The body of the FURIN$^{-/-}$ mice was smaller than that of the FURIN$^{+/+}$ and FURIN$^{+/-}$ mice at 3 months. **(D, E)** Western blot (D) and quantification (E) of furin protein in the cortex of FURIN$^{+/+}$ and FURIN$^{-/-}$ mice. **(F)** PCR gel bands show the presence of furin (350 bp) and the insertion of LOXP (395 bp) on the left, and Nestin-Cre (150 bp) on the right. **(G)** mRNA level of furin determined by RT-PCR in the FURIN$^{+/+}$ and FURIN$^{-/-}$ mice. **(H)** The survival rate in postnatal FURIN$^{+/+}$, FURIN$^{-/-}$, and FURIN$^{+/-}$ mice. $n = 50$ in each group. **(I)** Body weight comparison of the three different mice at the indicated days. $n = 50$ in each group (except $n = 24$ in the FURIN$^{-/-}$ mice at 180 days). *P*-values were calculated using two-tailed Student's *t*-test, ***$P < 0.005$, ****$P < 0.001$.

Loss of furin in the nervous system resulted in hydrocephalus

To determine whether furin deficiency might cause anatomical changes in the brain, we assessed brain morphology using magnetic resonance T2-weighted imaging. The coronary magnetic resonance images showed that compared with FURIN$^{+/+}$ mice, FURIN$^{+/-}$ mice had some degree of the lateral ventricle (LV) and third ventricle (TV) enlargement, whereas the aqueduct (Aq) and fourth ventricle (FV) were slightly enlarged, and had no significant morphological changes in Aq, FV, and the corpus callosum

(Fig. 2A). In FURIN$^{-/-}$ mice, the LV and TV are significantly enlarged, and the CSF-filled LVs coalesced into a vast single void (Fig. 2A); whereas the Aq was significantly narrowed, and the volume and shape of FV were relatively preserved (Fig. 2A). It is reported that the TV-Aq-FV axis is the narrowest portion of the entire ventricular system, in which the obstruction is the most frequent cause of hydrocephalus.[2,28] Median-sagittal magnetic resonance images showed that the Aqs were almost invisible in FURIN$^{-/-}$ mice (Fig. 2B). Accordingly, a stenotic Aq was clearly found by HE

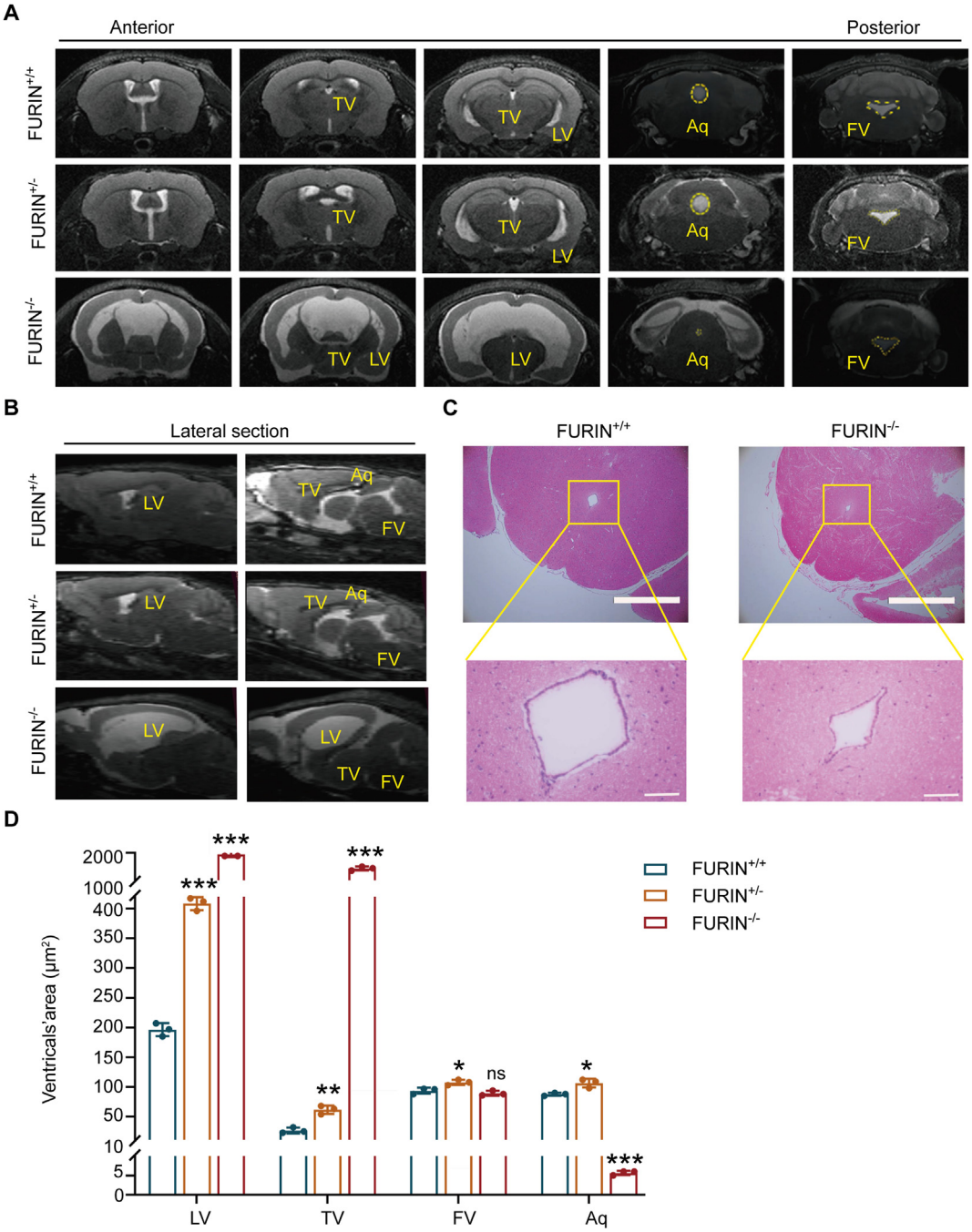

Figure 2 FURIN$^{-/-}$ mice develop postnatal hydrocephalus. **(A)** T2-weighted coronal magnetic resonance images of the brains of FURIN$^{+/+}$, FURIN$^{+/-}$, and FURIN$^{-/-}$ mice at 5 months. From left to right are in the order of forebrain to hindbrain. In the FURIN$^{-/-}$ mice, LV and TV were significantly enlarged, Aq was narrowed, and there was no significant difference in FV. LV, lateral ventricle; TV, third ventricle; Aq, aqueduct; FV, fourth ventricle. **(B)** T2-weighted sagittal magnetic resonance images of the brains at 5 months. In the FURIN$^{-/-}$ mice, LV and TV were significantly enlarged, and Aq was faintly visible. **(C, D)** The representative coronal HE sections of aqueduct in the FURIN$^{+/+}$ and FURIN$^{-/-}$ mice at 5 months. Scale bars: top, 500 μm; bottom, 50 μm. **(E)** Quantitative analysis of ventricles and catheters from (A). The data were expressed as mean ± standard error of the mean; *p*-values were calculated using two-tailed Student's *t*-test; NS, not significant; $^{*}P < 0.05$, $^{**}P < 0.01$, $^{***}P < 0.005$.

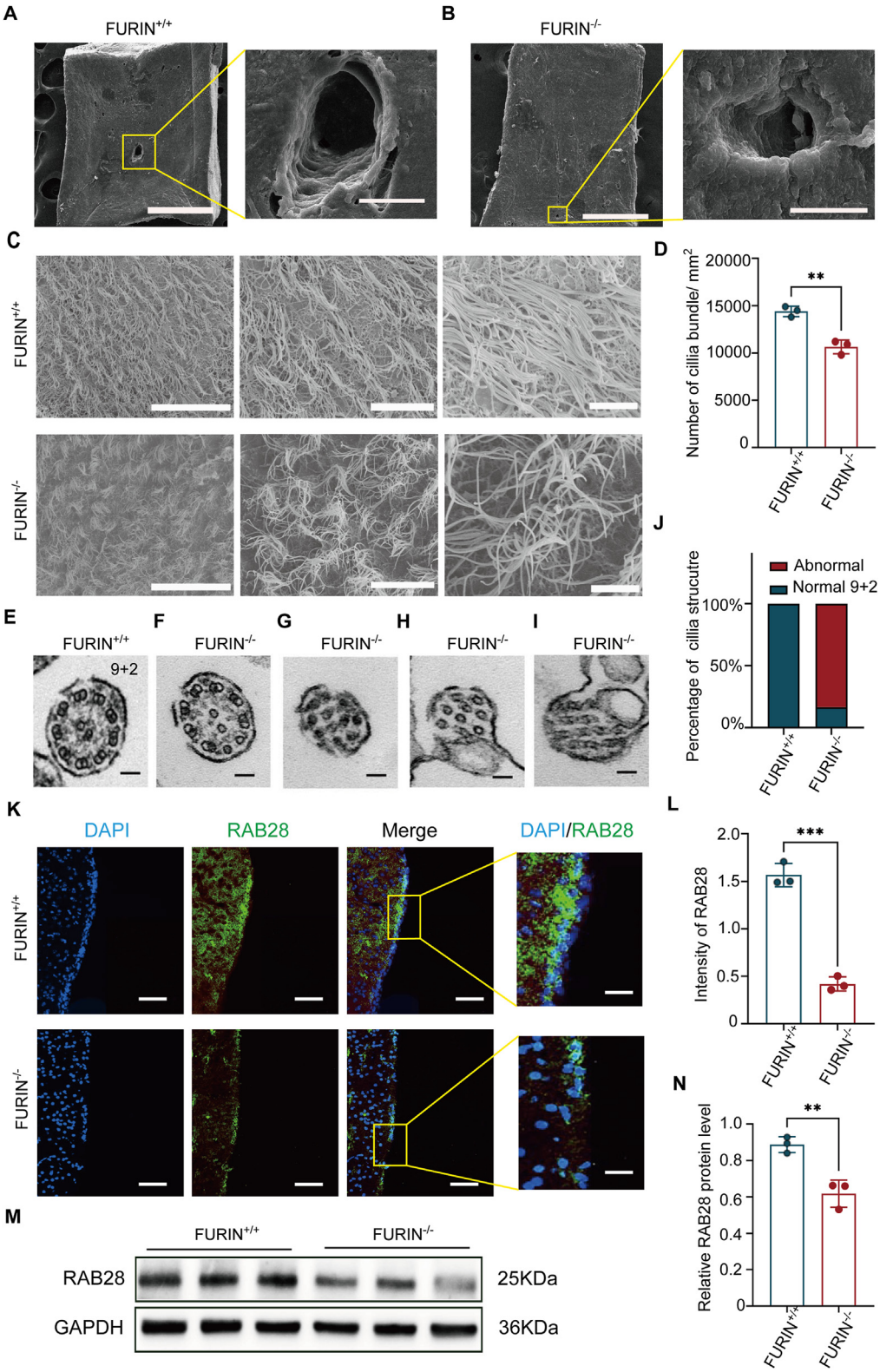

Figure 3 Cilial morphogenesis is disrupted with the decreased expression of RAB28 in FURIN$^{-/-}$ mice. **(A)** Representative SEM images show the aqueduct in the FURIN$^{+/+}$ mice at 5 months. Scale bars: 500 μm and 50 μm, respectively. **(B)** Representative SEM images show the aqueduct in the FURIN$^{-/-}$ mice at 5 months. Scale bars: 500 μm and 20 μm, respectively. **(C, D)** SEM images (C) and quantification (D) of ependymal cilia on the surface of lateral ventricles at 5 months. Evenly distributed cilium bundles with a uniformed direction of cilia tufts were presented in the FURIN$^{+/+}$ mice, whereas the sparsely distributed cilium bundles with shorter and fewer cilia in disrupted orientation were found in the FURIN$^{-/-}$ mice at 5 months. Scale bars: left, 50 μm; middle, 20 μm; right, 5 μm. **(E—J)** TEM images (E—I) and quantification (J) of microtubule organization with or without normal "9 + 2"

staining in FURIN$^{-/-}$ mice (Fig. 2C). As shown in Figure 2D, the average areas of LVs and TVs were dramatically increased in FURIN$^{+/-}$ and FURIN$^{-/-}$ mice than those in FURIN$^{+/+}$ mice, with the needle-like Aq and a relatively preserved FV. These results indicated that partial or complete loss of furin caused hydrocephalus during brain development.

Furin deficiency impaired ciliogenesis and down-regulated RAB28 expression

The Aq stenosis suggested pathological changes in the interface between CSF and the parenchyma. Indeed, the SEM image showed a normal shape and smooth lining of Aq in FURIN$^{+/+}$ mice, whereas a narrowed and slightly distorted Aq was found in FURIN$^{-/-}$ mice with some granulations on the wall (Fig. 3A, B). It is reported that dysfunctional cilia could disrupt CSF circulation with the collapsed Aq.[29,30] Thus, we assessed the morphology of cilia on the lateral ventricular wall using SEM. As shown in Figure 3C and D, compared with FURIN$^{+/+}$ mice that comprised a confluent ependymal cilial layer, FURIN$^{-/-}$ mice exhibited comparatively sparse cilium coverage. In FURIN$^{+/+}$ mice, the cilia were clustered and relatively aligned, with multi-clusters consistently orientated, whereas in FURIN$^{-/-}$ mice, the cilia clusters were disorganized in different directions, and distributed sparsely (Fig. 3C, D). Further TEM analysis revealed that the residual cilia retained a normal and classic (9 + 2) microtubule structure arrangement in FURIN$^{+/+}$ mice[31]; in comparison, the organization of microtubules was lost, and the numbers changed in different cilia sections of FURIN$^{-/-}$ mice (Fig. 3E—J). These results indicated that the structure and function of cilia were significantly impaired in furin-deficient mice.

Ciliogenesis is a multi-step process, in which membrane trafficking plays an essential role.[32] It is reported that the GTPase RAB28 is located in the endosomal pathway and contributes to ciliogenesis.[33] Given that furin regulates its target protein function in the Golgi and secretary vesicle compartments,[7] we speculated that the impaired ciliogenesis in furin cKO mice could be associated with RAB28 dysfunction. As shown in Figure 3K and L, the expression level of RAB28 was significantly decreased in the ependymal line of ventricles in furin cKO mice relative to the control. Accordingly, the protein level of RAB28 was also significantly decreased in the cortex of furin cKO mice (Fig. 3M, N). Thus, the reduced RAB28 could be suggestive of aberrant membrane trafficking by furin deficiency.

FURIN$^{-/-}$ mice exhibited neuronal loss and ependymal cell damage

To determine whether furin deficiency causes neuronal loss, we assessed the expression of NeuN,[34] a neuronal marker in the brain of furin cKO mice. As shown in Figure 4A and B, the NeuN-positive cells were significantly reduced in the brain of furin cKO mice relative to the control. Accordingly, the immunofluorescent staining of furin that formed a dotted line in ependyma was also significantly decreased in FURIN$^{-/-}$ mice (Fig. 4C, D).

Ependymal cells that are located in the wall of the LVs play an important role in hydrocephalus.[2] Moreover, ependymal cell differentiation is closely associated with ciliogenesis.[5,35] We speculate that the dysfunctional ciliogenesis might be accompanied by the impaired structural integrity of ependyma. Thus, we assessed the expression of ependymal cell marker S100β[36] in furin cKO mice. As shown in Figure 4E and F, the intensity of S100β was significantly reduced in FURIN$^{-/-}$ mice relative to FURIN$^{+/+}$ mice; and the S100β-labelled cells showed less connectivity, suggesting an impaired structural integrity of ependyma. As ADCY3 and PTBP1 are also indicative of cilia and ependymal cells,[37] respectively, we further found that the protein levels of ADCY3 and PTBP1 were significantly reduced in the brain of furin deficient mice (Fig. 4G, H). Accordingly, the protein levels of furin and S100β were significantly reduced in furin-deficient mice relative to the control (Fig. 4G, H). These results indicated that the damaged ependymal cells were accompanied by neuronal loss in the brain of furin cKO mice.

Proteomics signatures in the cortex of FURIN$^{-/-}$ mice

To further understand the potential molecular alterations induced by furin deficiency, we performed proteomics analysis using the cortical samples from FURIN$^{-/-}$ and FURIN$^{+/+}$ mice. A total of 5,895 proteins and 36,158 peptides were identified (Table S1). We found 49 differentially expressed proteins (DEPs) between FURIN$^{+/+}$ and FURIN$^{-/-}$ (P value < 0.05 and fold change >1.2 or < 0.83), which included 31 up-regulated and 18 down-regulated proteins (Fig. 5A). Gene ontology analysis revealed that "cell adhesion" was commonly enriched in the molecular function, cellular component, and biological process (Fig. 5B). As shown in Figure 5C, the heatmap depicted a detailed DEP list, in which L1cam and Dlg5 have been reported to cause hydrocephalus.[38,39] Kyoto Encyclopedia of Genes and Genomes analysis showed that these DEPs were enriched in 20 pathways; and again, "cell adhesion molecules" remained one of the most enriched (Fig. 5D). These DEPs were then mapped to Search Tool for the Retrieval of Interacting Genes/Proteins database for potential protein—protein interactions, which showed that integrin subunit beta 8 (ITGB8), fibrinogen alpha chain (FGA), and breast cancer anti-estrogen resistance 1 (BCAR1) were closely interacted (Fig. 5E). Western blotting analysis revealed that the increased expression of ITGB8 and the decreased levels of FGA and BCAR1 were found in FURIN$^{-/-}$ mice relative to

ultrastructure in the FURIN$^{+/+}$ and FURIN$^{-/-}$ mice at 5 months. **(K, L)** Immunofluorescent staining (K) and quantification (L) of RAB28 in ependymal cells of FURIN$^{+/+}$ and FURIN$^{-/-}$ mice at 5 months. Green, RAB28; blue, DAPI (nuclear marker). Scale bars: 20 μm. **(M, N)** Western blot images (M) and quantification (N) of RAB28 in the cortex of the FURIN$^{+/+}$ and FURIN$^{-/-}$ mice at 5 months. The data were expressed as mean ± standard error of the mean; p-values were calculated using two-tailed Student's t-test; *$P < 0.05$, ***$P < 0.005$.

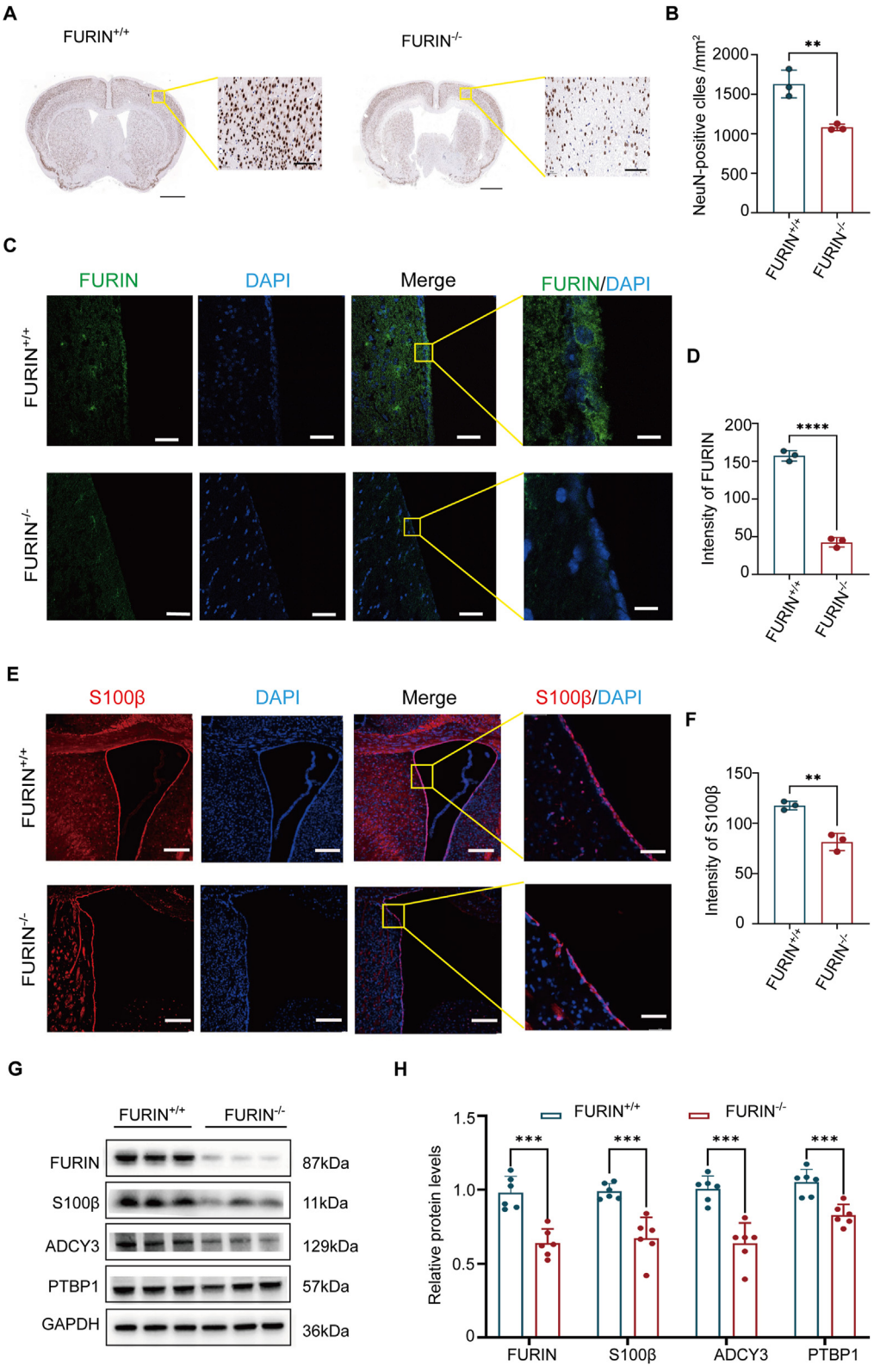

Figure 4 Neuronal loss went with the damaged ependymal cells in the FURIN$^{-/-}$ mice. **(A, B)** Coronal sections of immunohistochemical images of NeuN staining (A), and the corresponding quantification of NeuN-positive cell number (B) in the brain at 5 months. Scale bars: 1 mm and 50 μm, respectively. **(C, D)** Immunofluorescent staining (C) and quantification (D) of furin in ependymal cells of the FURIN$^{+/+}$ and FURIN$^{-/-}$ mice at 5 months. Green, furin; blue, DAPI (nuclear marker). Scale bars: 100 μm and 20 μm, respectively. **(E, F)** Immunofluorescent staining (E) and quantification (F) of S100β in the FURIN$^{+/+}$ and FURIN$^{-/-}$ mice at 5 months. Red, S100β (ependymal cell marker); blue, DAPI (nuclear marker). Scale bars: 200 μm and 50 μm, respectively. **(G, H)** Western blot images (G) and quantification (H) of furin, S100β, ADCY3, and PTBP1 in the cortex of FURIN$^{+/+}$ and FURIN$^{-/-}$ mice at 5 months. The data were expressed as mean ± standard error of the mean; *p*-values were calculated using two-tailed Student's *t*-test; $^{*}P < 0.05$; $^{**}P < 0.01$; $^{***}P < 0.005$.

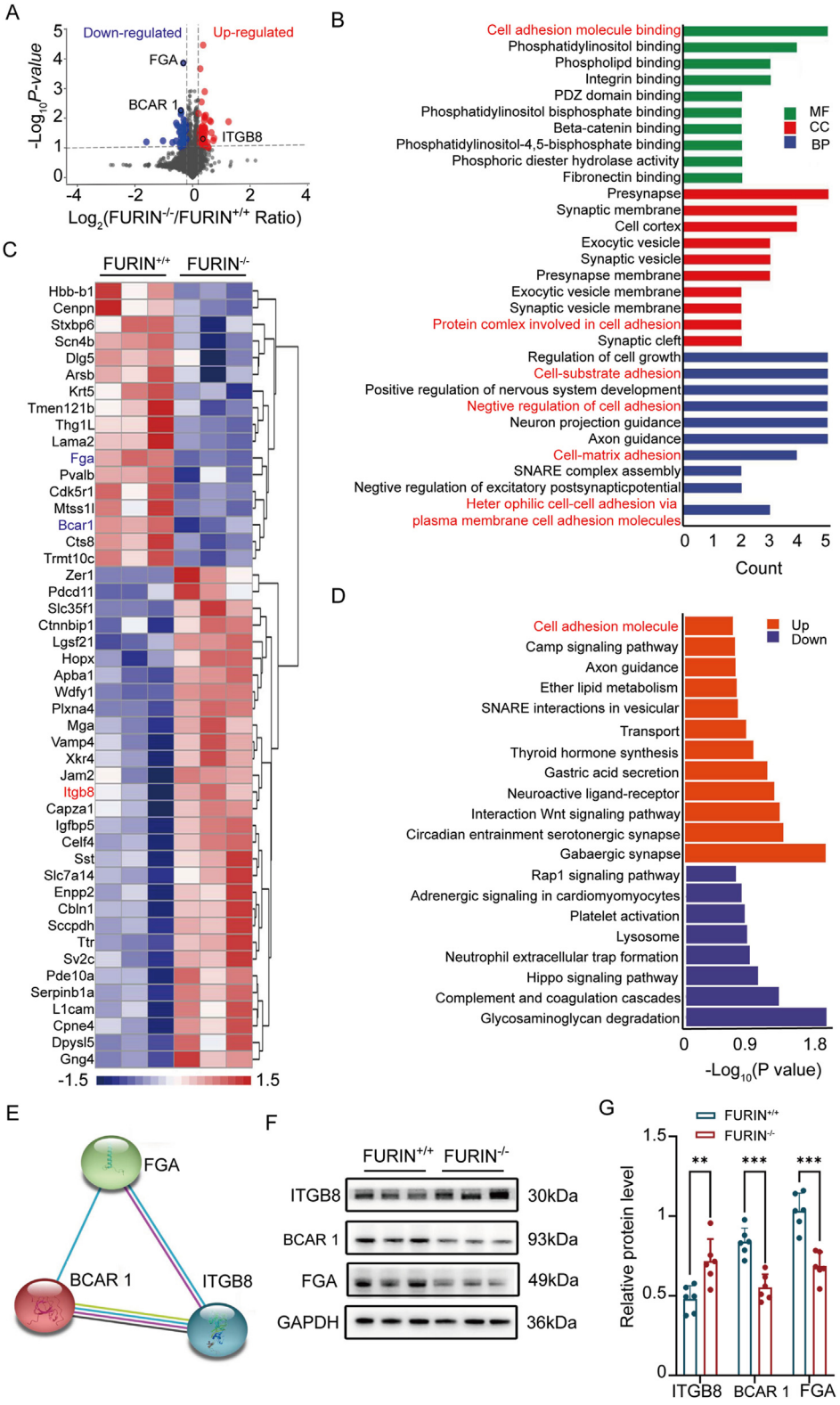

Figure 5 Proteomic signatures of furin deficiency. **(A)** Volcano plots of differentially expressed proteins (DEPs) in the cortex of the FURIN$^{-/-}$ mice relative to the FURIN$^{+/+}$ mice at 5 months. The red and blue points represent the up-regulated and down-regulated proteins with significant differences, respectively. **(B)** Gene ontology analysis for the identified 49 DEPs annotated into molecular function (MF), biological process (BP), and cellular component (CC). **(C)** Clustering heatmap for DEPs in the cortex of the FURIN$^{-/-}$ and FURIN$^{+/+}$ mice. The red and blue points represent up-regulated and down-regulated DEPs. **(D)** Kyoto Encyclopedia of Genes and Genomes pathway classification of the DEPs. **(E)** Protein–protein network enrichment analysis by Search Tool for the Retrieval of Interacting Genes/Proteins revealed that ITGB8, BCAR1, and FGA interacted. **(F, G)** Representative Western blot (F) and quantification (G) of ITGB8, BCAR1, and FGA in the cortex of mice at 5 months. The data were expressed as mean ± standard error of the mean; *P*-values were calculated using two-tailed Student's *t*-test; $^{**}P < 0.01$, $^{***}P < 0.005$.

FURIN$^{+/+}$ mice (Fig. 5F, G), demonstrating a good reliability and validity of proteomics. These results indicated that cell adhesion molecules were among the prominent proteomics signatures of furin deficiency.

Furin deletion facilitated astrocyte reactivity but not differentiation

Among the signature proteins that were changed in furin cKO mice, ITGB8 and BCAR1 are highly enriched astrocytes relative to neurons.[40,41] Given that adhesion molecules are known to regulate astrocyte morphology,[42] we speculated that astrocytic functions could be accordingly affected in furin cKO mice. As shown in Figure 6A, B, a widespread enhancement of GFAP, a marker of astrocyte,[43] was detected in the coronary sections of FURIN$^{-/-}$ mice (Fig. 6A, B). Especially, a dramatic augmentation of GFAP staining was distributed in the surrounding area of Aq, which was significantly narrowed in FURIN$^{-/-}$ mice relative to FURIN$^{+/+}$ mice (Fig. 6C, D). It is reported that astrocytes compensate for the loss of ependymal cells in hydrocephalus,[44] and SOX9, the specific marker of astrocyte,[45] is also indicative of glial precursor cells responsible for the generation of ependyma.[46,47] We next assessed the expression of SOX9 in the ependyma of furin cKO mice. As shown in Figure 6E and F, the immuno-signals of SOX9 were significantly reduced in FURIN$^{-/-}$ mice relative to FURIN$^{+/+}$ mice. The altered protein expression of GFAP and SOX9 was further confirmed by Western blotting analysis (Fig. 6G, H). These results indicated that astrocyte overgrowth went with a compromised differentiation into ependymal cells.

Discussion

CSF is mainly secreted by the choroid plexus epithelium, flows from the cerebral ventricles to subarachnoid spaces, and reaches the venous system through the glymphatic (glial-lymphatic) pathway.[48] In this pathway, CSF moves into the parenchyma along perivascular spaces, merges with interstitial fluid (ISF), and drains into the lymphatic system.[49,50] Between the ventricles and parenchyma, ependymal cells form a line and barrier.[51] It is reported that about 20% of CSF arises from ISF,[52] suggesting the role of ependymal cells in ISF-CSF interchange.[53] In the current study, we provide evidence that FURIN$^{-/-}$ mice develop progressive hydrocephalus, which is apparently accompanied by disorganized cilia and associated down-regulation of RAB28. Moreover, the altered protein levels, particularly adhesion molecules, are suggestive of astroglial reactivity with the compromised differentiation into ependymal cells.

Multiple motile cilia are found on the surface of ependymal cells, which promote the directed CSF circulation.[30,54] Hydrocephalus is caused by a mutation in Ccdc39 that controls cilial development, or lack of the adherins Celsr2 and Celsr3 that regulate ependymal ciliogenesis.[55,56] During ciliogenesis, the basal body is matured from a mother centriole and moves towards the plasma membrane; and this process involves the GTPase RAB28 that is localized to an intermediary ciliary vesicle.[57] It is reported that mutation in RAB28 prevents its localization to primary cilium,[58] and importantly, causes missing and disconnected axoneme in neuronal cells.[59] Moreover, the endocytic recycling pathway has been identified as one of the modulators of ciliogenesis,[60] which is in line with the function of furin that is trafficked between Golgi apparatus and cell surface,[7] and the important role of RAB28 in intracellular trafficking of endocytosed proteins.[33] In the present study, the Aq stenosis is accompanied by disorganized (9 + 2) microtubule structures and cilia orientation, and the decreased expression of ependymal RAB28 in Furin$^{-/-}$ mice, implying that an intracellular vesicle-turnover mechanism could contribute to the impaired ciliogenesis by furin.

Ependymal cells are essential for neuronal development.[61] It is reported that hydrocephalus can be caused by mutations in MPDZ gene that leads to ependymal malformation,[62] and by deletion of SNX27 or YAP that impairs ependymal cell differentiation.[37,63] Importantly, in mutant hydrocephalus with hop gait (hyh) mice,[64] ependymal denudation develops before the onset of hydrocephalus.[65] Although direct evidence is lacking, disruption of the ependymal barrier might favor ISF efflux into CSF in the ventricles, which are in close proximity to white matter.[66] As epithelial cells in the choroid plexus have a similar function to ependymal cells, structural defects of the choroid plexus could also increase CSF production.[67,68] In the current study, the decreased expression of ependymal markers S100β, ADCY3, and PTBP1 is paralleled by morphologically disintegrated ependymal cells, suggesting that the altered CSF dynamics induced by furin deficiency is closely associated with the impaired structure and function of ependymal cells. In line with ependymal denudation, a widespread loss of neuronal cells is presented in the brain of furin cKO mice. This could occur in a cell-autonomous manner, as furin overexpression promotes dendritic morphogenesis and learning and memory.[14] Importantly, neuronal loss may also lead to gliosis, as astrocytes respond to all forms of insults in the brain.[69] For instance, ischemic neuronal death is followed by rapid and severe astrocytosis[70]; and conversely, a reduction of neuronal loss is accompanied by decreased gliosis in the brain of Alzheimer's disease after mitochondrial transfer.[71]

The role of astrocytes in hydrocephalus is not conclusive.[72] It is reported that in an animal model of hyh mice, astrocytes form a layer at the denuded ventricular lining,[44] supporting that astroglial reaction may compensate for the loss of CSF homeostasis.[73] However, in a mouse model of Bardet—Biedl syndrome (BBS) caused by BBS8 deletion, the enhanced GFAP protein correlates with the development of hydrocephalus,[74] suggesting that astrocytes play a role in causing this phenotype. In our study, proteomics study reveals that cell adhesion molecules including astrocyte-enriched ITGB8 and BCAR1 are differentially regulated in furin cKO mice. As a member of the integrin family that plays an important role in brain assembly,[75] ITGB8 also regulates angiogenesis and embryo implantation.[76,77] In the radial glia, ITGB8 contributes to the expansion of the human brain during development[78]; and the function of the decreased FGA is supported by that FGA-KO facilitates the growth and metastasis of lung cancer through integrin-AKT signaling.[79] It could be likely that these changes are associated with enhanced GFAP staining and astrocytic overgrowth (Fig. 5C—E). On the other hand, BCAR1 (p130Cas), a member of the Crk-associated substrate family of scaffold

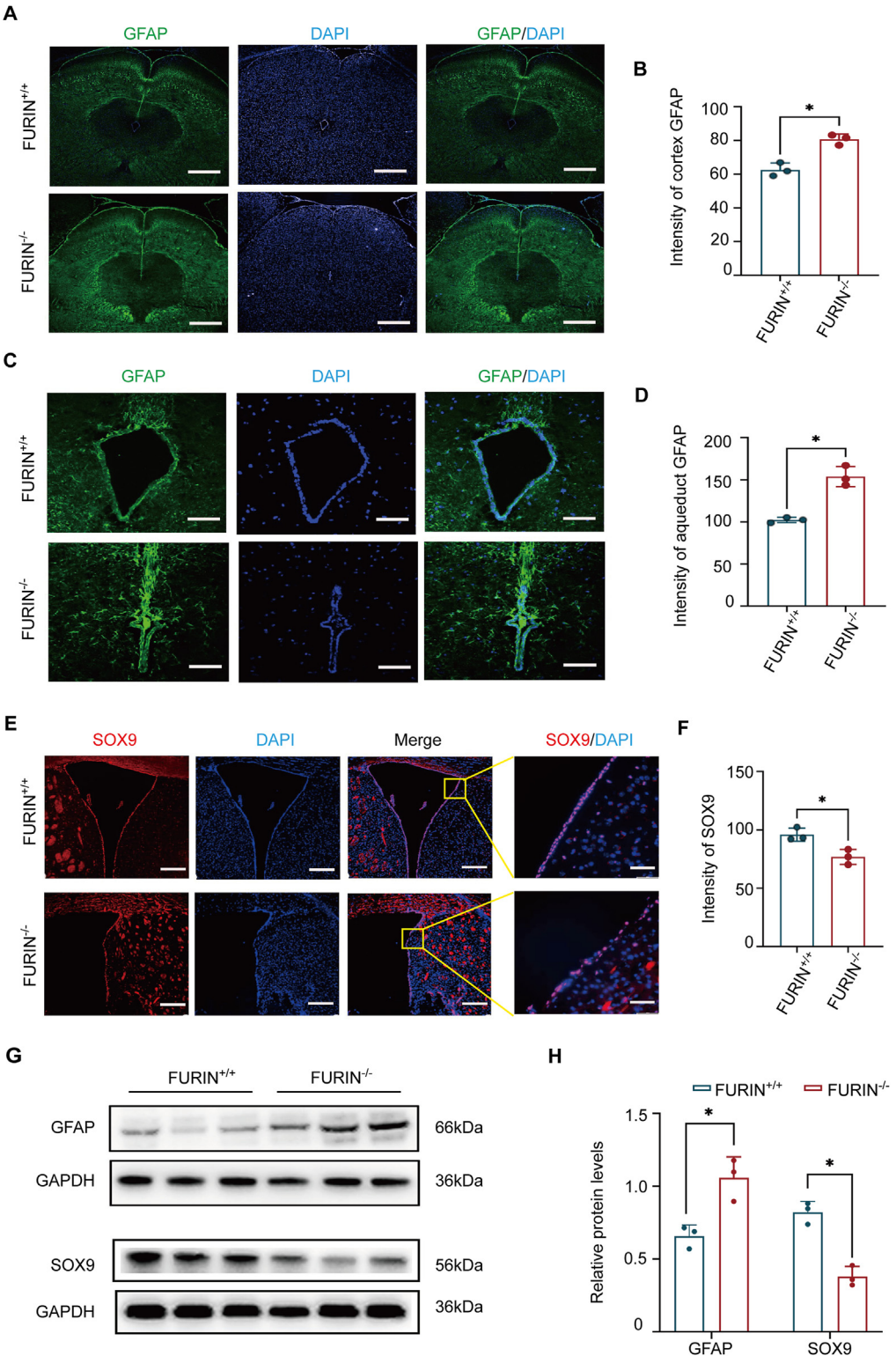

Figure 6 Furin deficiency promotes astrocyte overgrowth but not differentiation. **(A, B)** Immunofluorescent staining (A) and quantification (B) of GFAP in the whole brain (coronal section) of the FURIN$^{+/+}$ and FURIN$^{-/-}$ mice at 5 months. Green, GFAP (astrocyte marker); blue, DAPI (nuclear marker). Scale bars: 500 μm. **(C, D)** Immunofluorescent staining (C) and quantification (D) of GFAP in the aqueduct area of the FURIN$^{+/+}$ and FURIN$^{-/-}$ mice at 5 months. Green, GFAP (astrocyte marker); blue, DAPI (nuclear marker). Scale bars: 100 μm. **(E, F)** Immunofluorescent staining (E) and quantification (F) of SOX9 in the FURIN$^{+/+}$ and FURIN$^{-/-}$ mice at 5 months. Red, SOX9 (glia progenitor marker); blue, DAPI (nuclear marker). Scale bars: 200 μm and 50 μm, respectively. **(G, H)** Representative Western blot (G) and quantification (H) of GFAP and SOX9 in the FURIN$^{+/+}$ and FURIN$^{-/-}$ mice at 5 months. The data were expressed as mean ± standard error of the mean; *P*-values were calculated using two-tailed Student's *t*-test; $^{*}P < 0.05$.

proteins, controls neuronal outgrowth and axonal guidance.[80] By analogue, deletion of BCAR1 impairs the formation of dental enamel in mice and the caudal vein plexus in zebrafish,[81,82] the decreased expression of BCAR1 (Fig. 5F, G) could be associated with the impaired differentiation of astrocytic progenitor cells into ependymal cells. In support, the expression of SOX9 which is indicative of glial progenitor differentiation into mature ependyma[46,54] is significantly reduced in furin cKO mice. Given that astrocytes overgrow but fail to normally differentiate into ependymal cells, the present study supports that the dysfunctional astrocytes could play a role in the development of hydrocephalus.

In conclusion, through investigation of cerebral furin cKO mice, we have confirmed the previous findings that an impaired ciliogenesis of ependymal cells is a common feature of hydrocephalus. Whereas the proteomics results provide a clue for further understanding furin functions, the decreased expression of RAB28 associated with ciliogenesis and the disturbed differentiation of astrocytes into ependyma are highlighted in the present study.

Author contributions

GJ Chen and JR Zhou designed the study. SQ Xie and XY Xie cooperatively performed the experiments and analyzed the data. J Tang, B Luo, J Chen, QX Wen, L Song, GF Zhou, X Chen, L Chen, and Y Liu provided assistance to the research. GJ Chen and SQ Xie wrote the manuscript.

Conflict of interests

The authors declare no competing interests.

Funding

This work was supported by grants from the National Natural Science Foundation of China (No. 81971030, 82271461 to GJ Chen).

Appendix A. Supplementary data

Supplementary data to this article can be found online at https://doi.org/10.1016/j.gendis.2023.04.037.

References

1. Munch TN, Rostgaard K, Rasmussen ML, Wohlfahrt J, Juhler M, Melbye M. Familial aggregation of congenital hydrocephalus in a nationwide cohort. *Brain*. 2012;135(Pt 8):2409–2415.
2. Kahle KT, Kulkarni AV, Limbrick DD, Warf BC. *Hydrocephalus* in children. *Lancet*. 2016;387(10020):788–799.
3. Zhang J, Williams MA, Rigamonti D. Genetics of human hydrocephalus. *J Neurol*. 2006;253(10):1255–1266.
4. McAllister JP. Pathophysiology of congenital and neonatal hydrocephalus. *Semin Fetal Neonatal Med*. 2012;17(5):285–294.
5. Ji W, Tang Z, Chen Y, et al. Ependymal *cilia*: physiology and role in *hydrocephalus*. *Front Mol Neurosci*. 2022;15, 927479.
6. Nakayama K. Furin: a mammalian subtilisin/Kex2p-like endoprotease involved in processing of a wide variety of precursor proteins. *Biochem J*. 1997;327(Pt 3):625–635.
7. Thomas G. Furin at the cutting edge: from protein traffic to embryogenesis and disease. *Nat Rev Mol Cell Biol*. 2002;3(10):753–766.
8. Fitzgerald K. Furin protease: from SARS CoV-2 to *Anthrax, diabetes,* and hypertension. *Perm J*. 2020;24:20–187.
9. Osman EEA, Rehemtulla A, Neamati N. Why all the fury over furin? *J Med Chem*. 2022;65(4):2747–2784.
10. Braun E, Sauter D. Furin-mediated protein processing in infectious diseases and cancer. *Clin Transl Immunology*. 2019;8(8), e1073.
11. Ren K, Jiang T, Zheng XL, Zhao GJ. Proprotein convertase furin/PCSK3 and atherosclerosis: new insights and potential therapeutic targets. *Atherosclerosis*. 2017;262:163–170.
12. Hwang EM, Kim SK, Sohn JH, et al. Furin is an endogenous regulator of α-secretase associated APP processing. *Biochem Biophys Res Commun*. 2006;349(2):654–659.
13. Zhang Y, Gao X, Bai X, Yao S, Chang YZ, Gao G. The emerging role of furin in neurodegenerative and neuropsychiatric diseases. *Transl Neurodegener*. 2022;11(1):39.
14. Zhu B, Zhao L, Luo D, et al. Furin promotes dendritic morphogenesis and learning and memory in transgenic mice. *Cell Mol Life Sci*. 2018;75(13):2473–2488.
15. Yang Y, He M, Tian X, et al. Transgenic overexpression of furin increases epileptic susceptibility. *Cell Death Dis*. 2018;9(11):1058.
16. Scamuffa N, Calvo F, Chrétien M, Seidah NG, Khatib AM. Proprotein convertases: lessons from knockouts. *Faseb J*. 2006;20(12):1954–1963.
17. Bernal A, Arranz L. Nestin-expressing progenitor cells: function, identity and therapeutic implications. *Cell Mol Life Sci*. 2018;75(12):2177–2195.
18. Sclafani AM, Skidmore JM, Ramaprakash H, Trumpp A, Gage PJ, Martin DM. Nestin-Cre mediated deletion of Pitx2 in the mouse. *Genesis*. 2006;44(7):336–344.
19. Hu XT, Zhu BL, Zhao LG, et al. Histone deacetylase inhibitor apicidin increases expression of the α-secretase ADAM10 through transcription factor USF_1-mediated mechanisms. *Faseb J*. 2017;31(4):1482–1493.
20. Wen QX, Luo B, Xie XY, et al. AP2S1 regulates APP degradation through late endosome-lysosome fusion in cells and APP/PS1 mice. *Traffic*. 2023;24(1):20–33.
21. Im K, Mareninov S, Diaz MP, Yong WH. An introduction to performing immunofluorescence staining. *Methods Mol Biol*. 2019;1897:299–311.
22. Valnes K, Brandtzaeg P. Paired indirect immunoenzyme staining with primary antibodies from the same species. Application of horseradish peroxidase and alkaline phosphatase as sequential labels. *Histochem J*. 1984;16(5):477–487.
23. Cohen AR, Leifer DW, Zechel M, Flaningan DP, Lewin JS, Lust WD. Characterization of a model of hydrocephalus in transgenic mice. *J Neurosurg*. 1999;91(6):978–988.
24. Nagashima K, Zheng J, Parmiter D, Patri AK. Biological tissue and cell culture specimen preparation for TEM nanoparticle characterization. *Methods Mol Biol*. 2011;697:83–91.
25. Nowell JA, Pawley JB. Preparation of experimental animal tissue for SEM. *Scanning Electron Microsc*. 1980;(pt 2):1–19.
26. Ma L, Du Y, Xu X, et al. β-catenin deletion in regional neural progenitors leads to congenital *Hydrocephalus* in mice. *Neurosci Bull*. 2022;38(1):81–94.
27. Lakso M, Pichel JG, Gorman JR, et al. Efficient *in vivo* manipulation of mouse genomic sequences at the zygote stage. *Proc Natl Acad Sci U S A*. 1996;93(12):5860–5865.
28. Banizs B, Pike MM, Millican CL, et al. Dysfunctional cilia lead to altered ependyma and choroid plexus function, and result in

the formation of hydrocephalus. *Development*. 2005;132(23):5329–5339.
29. Del Bigio MR. Ependymal cells: biology and pathology. *Acta Neuropathol*. 2010;119(1):55–73.
30. Kumar V, Umair Z, Kumar S, Goutam RS, Park S, Kim J. The regulatory roles of motile cilia in CSF circulation and hydrocephalus. *Fluids Barriers CNS*. 2021;18(1):31.
31. Satir P, Christensen ST. Overview of structure and function of mammalian cilia. *Annu Rev Physiol*. 2007;69:377–400.
32. Zhao H, Khan Z, Westlake CJ. Ciliogenesis membrane dynamics and organization. *Semin Cell Dev Biol*. 2023;133:20–31.
33. Lumb JH, Leung KF, Dubois KN, Field MC. Rab28 function in trypanosomes: interactions with retromer and ESCRT pathways. *J Cell Sci*. 2011;124(pt 22):3771–3783.
34. Wolf HK, Buslei R, Schmidt-Kastner R, et al. NeuN: a useful neuronal marker for diagnostic histopathology. *J Histochem Cytochem*. 1996;44(10):1167–1171.
35. Mitchell DR. Speculations on the evolution of 9+2 organelles and the role of central pair microtubules. *Biol Cell*. 2004;96(9):691–696.
36. Ohata S, Nakatani J, Herranz-Pérez V, et al. Loss of *Dishevelled*s disrupts planar polarity in ependymal motile *Cilia* and results in *Hydrocephalus*. *Neuron*. 2014;83(3):558–571.
37. Park R, Moon UY, Park JY, et al. Yap is required for ependymal integrity and is suppressed in LPA-induced hydrocephalus. *Nat Commun*. 2016;7, 10329.
38. Schäfer MKE, Altevogt P. L1CAM malfunction in the nervous system and human carcinomas. *Cell Mol Life Sci*. 2010;67(14):2425–2437.
39. Nechiporuk T, Fernandez TE, Vasioukhin V. Failure of epithelial tube maintenance causes *Hydrocephalus* and renal cysts in *Dlg5*$^{-/-}$ mice. *Dev Cell*. 2007;13(3):338–350.
40. Simpson JE, Ince PG, Shaw PJ, et al. Microarray analysis of the astrocyte transcriptome in the aging brain: relationship to Alzheimer's pathology and *APOE* genotype. *Neurobiol Aging*. 2011;32(10):1795–1807.
41. Yang J, Liu AY, Tang B, et al. Chronic nicotine differentially affects murine transcriptome profiling in isolated cortical interneurons and pyramidal neurons. *BMC Genom*. 2017;18(1):194.
42. Cho S, Muthukumar AK, Stork T, Coutinho-Budd JC, Freeman MR. Focal adhesion molecules regulate astrocyte morphology and glutamate transporters to suppress seizure-like behavior. *Proc Natl Acad Sci U S A*. 2018;115(44):11316–11321.
43. Brenner M, Messing A. Regulation of GFAP expression. *ASN Neuro*. 2021;13, 1759091420981206.
44. Roales-Buján R, Páez P, Guerra M, et al. Astrocytes acquire morphological and functional characteristics of ependymal cells following disruption of ependyma in hydrocephalus. *Acta Neuropathol*. 2012;124(4):531–546.
45. Sun W, Cornwell A, Li J, et al. SOX9 is an astrocyte-specific nuclear marker in the adult brain outside the neurogenic regions. *J Neurosci*. 2017;37(17):4493–4507.
46. Scott CE, Wynn SL, Sesay A, et al. SOX9 induces and maintains neural stem cells. *Nat Neurosci*. 2010;13(10):1181–1189.
47. Merkle FT, Tramontin AD, García-Verdugo JM, Alvarez-Buylla A. Radial glia give rise to adult neural stem cells in the subventricular zone. *Proc Natl Acad Sci U S A*. 2004;101(50):17528–17532.
48. Shapey J, Toma A, Saeed SR. Physiology of cerebrospinal fluid circulation. *Curr Opin Otolaryngol Head Neck Surg*. 2019;27(5):326–333.
49. Bohr T, Hjorth PG, Holst SC, et al. The glymphatic system: current understanding and modeling. *iScience*. 2022;25(9), 104987.
50. Rasmussen MK, Mestre H, Nedergaard M. The glymphatic pathway in neurological disorders. *Lancet Neurol*. 2018;17(11):1016–1024.
51. Jiménez AJ, Domínguez-Pinos MD, Guerra MM, Fernández-Llebrez P, Pérez-Fígares JM. Structure and function of the ependymal barrier and diseases associated with ependyma disruption. *Tissue Barriers*. 2014;2, e28426.
52. Shetty AK, Zanirati G. The interstitial system of the brain in health and disease. *Aging Dis*. 2020;11(1):200–211.
53. Hladky SB, Barrand MA. Mechanisms of fluid movement into, through and out of the brain: evaluation of the evidence. *Fluids Barriers CNS*. 2014;11(1):26.
54. Delgehyr N, Meunier A, Faucourt M, et al. Ependymal cell differentiation, from monociliated to multiciliated cells. *Methods Cell Biol*. 2015;127:19–35.
55. Abdelhamed Z, Vuong SM, Hill L, et al. A mutation in *Ccdc39* causes neonatal hydrocephalus with abnormal motile cilia development in mice. *Development*. 2018;145(1):dev154500.
56. Tissir F, Qu Y, Montcouquiol M, et al. Lack of cadherins Celsr2 and Celsr3 impairs ependymal ciliogenesis, leading to fatal hydrocephalus. *Nat Neurosci*. 2010;13(6):700–707.
57. Reiter JF, Leroux MR. Genes and molecular pathways underpinning ciliopathies. *Nat Rev Mol Cell Biol*. 2017;18(9):533–547.
58. Jespersgaard C, Hey AB, Ilginis T, et al. A missense mutation in RAB28 in a family with cone-rod dystrophy and postaxial polydactyly prevents localization of RAB28 to the primary *Cilium*. *Invest Ophthalmol Vis Sci*. 2020;61(2):29.
59. Jensen VL, Carter S, Sanders AA, et al. Whole-organism developmental expression profiling identifies RAB-28 as a novel ciliary GTPase associated with the BBSome and intraflagellar transport. *PLoS Genet*. 2016;12(12), e1006469.
60. Kim J, Lee JE, Heynen-Genel S, et al. Functional genomic screen for modulators of ciliogenesis and cilium length. *Nature*. 2010;464(7291):1048–1051.
61. Nelles DG, Hazrati LN. Ependymal cells and neurodegenerative disease: outcomes of compromised ependymal barrier function. *Brain Commun*. 2022;4(6):fcac288.
62. Saugier-Veber P, Marguet F, Lecoquierre F, et al. *Hydrocephalus* due to multiple ependymal malformations is caused by mutations in the *MPDZ* gene. *Acta Neuropathol Commun*. 2017;5(1):36.
63. Wang X, Zhou Y, Wang J, et al. SNX27 deletion causes *Hydrocephalus* by impairing ependymal cell differentiation and ciliogenesis. *J Neurosci*. 2016;36(50):12586–12597.
64. Bronson RT, Lane PW. *Hydrocephalus* with hop gait (*hyh*): a new mutation on chromosome 7 in the mouse. *Dev Brain Res*. 1990;54(1):131–136.
65. Jiménez AJ, Tomé M, Páez P, et al. A programmed ependymal denudation precedes congenital *Hydrocephalus* in the hyh mutant mouse. *J Neuropathol Exp Neurol*. 2001;60(11):1105–1119.
66. Rosenberg GA, Kyner WT, Estrada E. Bulk flow of brain interstitial fluid under normal and hyperosmolar conditions. *Am J Physiol*. 1980;238(1):F42–F49.
67. Benarroch EE. Choroid plexus–CSF system: recent developments and clinical correlations. *Neurology*. 2016;86(3):286–296.
68. Swiderski RE, Agassandian K, Ross JL, Bugge K, Cassell MD, Yeaman C. Structural defects in cilia of the choroid plexus, subfornical organ and ventricular ependyma are associated with ventriculomegaly. *Fluids Barriers CNS*. 2012;9(1):22.
69. Sofroniew MV. Molecular dissection of reactive astrogliosis and glial scar formation. *Trends Neurosci*. 2009;32(12):638–647.
70. Lee TK, Kim H, Song M, et al. Time-course pattern of neuronal loss and gliosis in gerbil hippocampi following mild, severe, or lethal transient global cerebral ischemia. *Neural Regen Res*. 2019;14(8):1394–1403.
71. Nitzan K, Benhamron S, Valitsky M, et al. Mitochondrial transfer ameliorates cognitive deficits, neuronal loss, and gliosis in Alzheimer's disease mice. *J Alzheimers Dis*. 2019;72(2):587–604.

72. Yang Y, Wang C, Chen R, et al. Novel therapeutic modulators of astrocytes for hydrocephalus. *Front Mol Neurosci*. 2022;15, 932955.
73. Varela MF, Miyabe MM, Oria M. Fetal brain damage in congenital hydrocephalus. *Childs Nerv Syst*. 2020;36(8): 1661—1668.
74. Singh M, Garrison JE, Wang K, Sheffield VC. Absence of BBSome function leads to astrocyte reactivity in the brain. *Mol Brain*. 2019;12(1):48.
75. Jaudon F, Thalhammer A, Cingolani LA. Integrin adhesion in brain assembly: from molecular structure to neuropsychiatric disorders. *Eur J Neurosci*. 2021;53(12):3831—3850.
76. De A, Morales JE, Chen Z, Sebastian S, McCarty JH. The β8 integrin cytoplasmic domain activates extracellular matrix adhesion to promote brain neurovascular development. *Development*. 2022;149(6), dev200472.
77. Kumar V, Maurya VK, Joshi A, Meeran SM, Jha RK. Integrin beta 8 (ITGB8) regulates embryo implantation potentially via controlling the activity of TGF-B1 in mice. *Biol Reprod*. 2015; 92(4):109.
78. Pollen AA, Bhaduri A, Andrews MG, et al. Establishing cerebral organoids as models of human-specific brain evolution. *Cell*. 2019;176(4):743—756.e17.
79. Wang M, Zhang G, Zhang Y, et al. Fibrinogen alpha chain knockout promotes tumor growth and metastasis through integrin-AKT signaling pathway in lung cancer. *Mol Cancer Res*. 2020;18(7):943—954.
80. del Pilar Camacho Leal M, Sciortino M, Tornillo G, Colombo S, Defilippi P, Cabodi S. p130Cas/BCAR1 scaffold protein in tissue homeostasis and pathogenesis. *Gene*. 2015;562(1):1—7.
81. Inoue A, Kiyoshima T, Yoshizaki K, et al. Deletion of epithelial cell-specific p130Cas impairs the maturation stage of amelogenesis. *Bone*. 2022;154, 116210.
82. Wisniewski L, French V, Lockwood N, Valdivia LE, Frankel P. P130Cas/bcar1 mediates zebrafish caudal vein plexus angiogenesis. *Sci Rep*. 2020;10(1), 15589.